Astronomy & Astrophysics

The *Herschel* Virgo Cluster Survey

IX. Dust-to-gas mass ratio and metallicity gradients in four Virgo spiral galaxies

L. Magrini[1], S. Bianchi[1], E. Corbelli[1], L. Cortese[3], L. Hunt[1], M. Smith[2], C. Vlahakis[4], J. Davies[2], G. J. Bendo[5], M. Baes[6], A. Boselli[7], M. Clemens[8], V. Casasola[9], I. De Looze[6], J. Fritz[6], C. Giovanardi[1], M. Grossi[10], T. Hughes[11], S. Madden[12], C. Pappalardo[1], M. Pohlen[2], S. di Serego Alighieri[1], and J. Verstappen[6]

[1] INAF – Osservatorio Astrofisico di Arcetri, Largo E. Fermi, 5, 50125 Firenze, Italy
   e-mail: laura@arcetri.astro.it
[2] Department of Physics and Astronomy, Cardiff University, The Parade, Cardiff, CF24 3AA, UK
[3] European Southern Observatory, Karl-Schwarzschild-Strasse 2, 85748 Garching bei München, Germany
[4] Departamento de Astronomia, Universidad de Chile, Casilla 36-D, Santiago, Chile
[5] Jodrell Bank Centre for Astrophysics, Alan Turing Building, School of Physics and Astronomy, University of Manchester, Manchester M13 9PL, UK
[6] Sterrenkundig Observatorium, Universiteit Gent, Krijgslaan 281 S9, 9000 Gent, Belgium
[7] Laboratoire d'Astrophysique de Marseille, UMR 6110 CNRS, 38 rue F. Joliot-Curie, 13388 Marseille, France
[8] Osservatorio Astronomico di Padova, Vicolo dell'Osservatorio 5, 35122 Padova, Italy
[9] INAF – Istituto di Radioastronomia, via P. Gobetti 101, 40129 Bologna, Italy
[10] CAAUL, Observatorio Astronomico de Lisboa, Universidade de Lisboa, Tapada de Ajuda, 1349-018 Lisboa, Portugal
[11] The Kavli Institute for Astronomy & Astrophysics, Peking University, Beijing 100871, PR China
[12] Service d'Astrophysique, CEA/Saclay, l'Orme des Merisiers, 91191 Gif-sur-Yvette, France

ABSTRACT

Context. Using *Herschel* data from the open time key project the *Herschel* Virgo Cluster Survey (HeViCS), we investigated the relationship between the metallicity gradients expressed by metal abundances in the gas phase as traced by the chemical composition of HII regions, and in the solid phase, as traced by the dust-to-gas mass ratio.
Aims. We derived the radial gradient of the dust-to-gas mass ratio for all galaxies observed by HeViCS whose metallicity gradients are available in the literature. They are all late type Sbc galaxies, namely NGC 4254, NGC 4303, NGC 4321, and NGC 4501.
Methods. We fitted PACS and SPIRE observations with a single-temperature modified blackbody, inferred the dust mass, and calculated two dimensional maps of the dust-to-gas mass ratio, with the total mass of gas from available HI and CO maps. HI moment-1 maps were used to derive the geometric parameters of the galaxies and extract the radial profiles. We examined different dependencies on metallicity of the CO-to-H_2 conversion factor (X_{CO}), used to transform the ^{12}CO observations into the amount of molecular hydrogen.
Results. We found that in these galaxies the dust-to-gas mass ratio radial profile is extremely sensitive to choice of the X_{CO} value, since the molecular gas is the dominant component in the inner parts. We found that for three galaxies of our sample, namely NGC 4254, NGC 4321, and NGC 4501, the slopes of the oxygen and of the dust-to-gas radial gradients agree up to $\sim$0.6−0.7 R_{25} using X_{CO} values in the range 1/3−1/2 Galactic X_{CO}. For NGC 4303 a lower value of $X_{CO} \sim 0.1 \times 10^{20}$ is necessary.
Conclusions. We suggest that such low X_{CO} values might be due to a metallicity dependence of X_{CO} (from close to linear for NGC 4254, NGC 4321, and NGC 4501 to superlinear for NGC 4303), especially in the radial regions $R_G < 0.6$−0.7 R_{25} where the molecular gas dominates. On the other hand, the outer regions, where the atomic gas component is dominant, are less affected by the choice of X_{CO}, and thus we cannot put constraints on its value there.

Key words. galaxies: spiral – galaxies: abundances – submillimeter: galaxies – galaxies: ISM – dust, extinction

1. Introduction

Virgo is one of the best studied galaxy clusters, being the richest cluster nearest to our own Galaxy (∼17 Mpc, Gavazzi et al. 1999). It is a relatively populous system, consisting of more than 1000 confirmed members (Binggeli et al. 1985). Galaxies in clusters such as Virgo differ significantly from their field counterparts since interactions with the hostile environment remove gas, quenching the star formation (cf., Boselli & Gavazzi 2006).

A galaxy's metallicity is closely related to the star formation (SF) history by which the interstellar medium (ISM) is enriched with the end-products of stellar evolution, and to the infall

process that dilutes the ISM and triggers new SF. As a consequence of their star formation histories, gas stripping and infall events, modified by the cluster environment, galaxies in clusters are expected also to differ in metal content relatively to isolated galaxies. A fundamental tool with which tracing the chemical evolution of a galaxy is the study of its radial metallicity gradient. The metallicity gradient tracks indeed the star formation history of galaxies, integrated over time, together with infall and/or outflow events.

The first pioneering work in Virgo was done by Skillman et al. (1996), who analyzed nine spiral galaxies with the aim of seeking correlations among their gas content, locations in the

cluster, metallicities and radial gradients, and comparing them with field spirals. Skillman et al. (1996) found weak evidence of shallower gradients in cluster galaxies deficient in HI than gradients in galaxies with a normal HI content. The situation is however very complex because galaxy interactions affect the star formation history and the gas content across the disk, producing metallicity gradients which differ from those measured in isolated galaxies of the same morphological type. Rupke et al. (2010) have shown that gradients in strongly interacting galaxies are flatter than in similar isolated galaxies; on the other hand, the metallicity gradient of M 81, the largest member of a small group of galaxies, is steeper than in an isolated counterpart due to gas removal in the outskirts (Stanghellini et al. 2010).

A direct correlation between gas metallicity and the dust-to-gas mass ratio is naturally expected since approximatively half of the metals in the ISM reside in dust grains; thus the dust-to-gas ratio should scale with metal abundance. Such a trend has been obtained theoretically by models computing consistently the evolution of metals and dust, despite the large uncertainties in the yields of both (Dwek 1998; Inoue 2003). The relation of the global dust-to-gas mass ratio with metallicity was investigated by, e.g., James et al. (2002); Draine et al. (2007); Hirashita et al. (2008); Lisenfeld & Ferrara (1998). The radial variation of the dust-to-gas mass ratio was first investigated by Issa et al. (1990) in our Galaxy and in other nearby galaxies (LMC, SMC, M 31, M 33, and M 51) who found evidence for a correlation, with dust-to-gas mass ratio and metallicity decreasing at roughly the same rate with increasing galactocentric radius. More recently, Boissier et al. (2004, 2005) and Thilker et al. (2007) found a clear relationship between metallicity and extinction, thus dust, in several nearby galaxies, suggesting that the variation in extinction is associated with the metallicity gradient. Muñoz-Mateos et al. (2009) found a good correlation between dust-to-gas and metallicity gradients in the *Spitzer* Infrared Nearby Galaxies Survey (SINGS; Kennicutt et al. 2003). Finally, Bendo et al. (2010a) compared the dust-to-gas ratio and metallicity gradients in NGC 2403, finding a similar decreasing behavior with radius.

We have recently obtained observations of the Virgo galaxies with the *Herschel* Space Observatory (Pilbratt et al. 2010), within the open time key project HeViCS (*Herschel* Virgo Cluster Survey) (Davies et al. 2010). HeViCS maps a wide area over the Virgo Cluster at wavelengths from 100 to 500 μm. This spectral range covers the peak of the thermal emission from cold dust ($T < 30$ K) which enables the detection of the bulk of the dust emission in galaxies. Also, *Herschel* gives an unprecedented resolution at these wavelengths (ranging from about 10″ to 36″, equivalent to $\sim 1-3$ kpc for Virgo galaxies). Atomic and molecular gas maps are available in the literature at a comparable resolution (Chung et al. 2009a; Kuno et al. 2007), thus providing resolved maps and the possibility of deriving radial gradients of dust-to-gas mass ratios.

In the present paper we assessed the validity of using HeViCS observations to obtain metallicity gradients from radial profiles of the dust-to-gas mass ratio. We investigated the hypothesis that the local dust-to-gas mass ratio is proportional to metallicity, starting from the four spiral galaxy in the Virgo cluster (NGC 4254, NGC 4303, NGC 4321, and NGC 4501) whose metallicity gradients are available in the literature. We studied the relation between radial profiles of metallicity and dust-to-gas mass ratios, and how this can be used to constrain the CO-to-H$_2$ conversion factor (X_{CO}) and its dependence on metallicity.

The paper is structured as follows: in Sect. 2 we describe the new HeViCS observations, and the observations of atomic and molecular gas. We also derive the oxygen abundance and its radial gradient in each galaxy. Section 3 discusses the fits to the observed *Herschel* dust spectral energy distributions (SEDs), how the radial profiles are derived, and how we calculate dust and gas masses. In Sect. 4 we develop the method by which we constrain X_{CO}, and Sect. 5 gives our conclusions.

2. Data

2.1. The sample

In the HeViCS field there are four galaxies for which the oxygen gradient has been well determined in the literature (e.g., Skillman et al. 1996; Moustakas et al. 2010). They are NGC 4254 (M 99), NGC 4303 (M 61), NGC 4321 (M 100), and NGC 4501 (M 88), all Sbc late-type galaxies.

NGC 4254 is a bright spiral galaxy located at the periphery of the Virgo cluster, at a projected distance of ~ 1 Mpc from the cluster center. Optical images show that this galaxy has one-armed structure, also seen in the HI gas distribution (Phookun et al. 1993; Chung et al. 2009a). Such an asymmetric spiral pattern is often observed in tidally galaxies, but there is no apparently massive companion near NGC 4254 (Sofue et al. 2003).

NGC 4321 is located at a distance of ~ 1.1 Mpc form M 87, and has an HI disk that is slightly larger than the optical disk.

NGC 4501 is the closest galaxy of our sample to M 87, being located at a distance of ~ 0.5 Mpc. It is weakly HI-deficient, following the definition of Chung et al. (2009a). Comparisons with simulations suggest that NGC 4501 is in an early stage of ram pressure stripping (Vollmer et al. 2008), entering the high-density region of the cluster for the first time.

NGC 4303 is the most isolated galaxy in our sample. It is a barred spiral galaxy with face-on geometry located in the outskirts of the Virgo cluster. We assume for all the galaxies the distance of ~ 17 Mpc (Gavazzi et al. 1999).

2.2. Herschel observations

The HeViCS program consists of *Herschel* observations of an area of about 60 sq. deg over the denser parts of the Virgo Cluster. The total area is made of 4 overlapping fields, which are observed in parallel scanning mode (*fast* scan rate: 60″/s) with both the PACS and SPIRE instruments, yielding data simultaneously in 5 spectral bands, at 100 and 160 μm (from PACS) and at 250, 350, and 500 μm (from SPIRE). At the completion of the program, each field will be covered with 8 scans done in two perpendicular scan directions. The full width half maximum (FWHM) of the beams is 6″98 × 12″7 and 11″64 × 15″65 in the two PACS bands (PACS observer's manual, 2010), and 18″2, 24″9, 36″3 in the three SPIRE bands (SPIRE observer's manual, 2010). At the time of writing, each field has been observed with at least two scans. In this paper, we use this dataset, whose data reduction and analysis is described in details in Paper VIII, Davies et al. (2011).

Some papers presenting *Herschel* observations for these galaxies have been already published. Eales et al. (2010) and Sauvage et al. (2010) analyzed the SPIRE maps of NGC 4254 (M 99) and NGC 4321 (M 100) observed within the *Herschel* Reference Survey (Boselli et al. 2010) to map the ISM using dust emission. Adding these data to archival *Spitzer*, HI, and CO maps, Pohlen et al. (2010) investigated the spatial distribution of gas and dust in these same galaxies. They also present

as a preliminary result, the ratio of the total gas mass ($HI + H_2$) to 500 μm flux, an approximation of the dust mass for the two galaxies. They found a decreasing dust-to-gas mass ratio with radius, consistent with results by, e.g., Bendo et al. (2010a) in NGC 2403. With the present-time availability of the PACS data the dust SED fitting can be better defined allowing to measure the exact shape of the radial dust-to-gas mass gradient. Finally, Smith et al. (2010) presented a resolved dust analysis of three of the largest (in angular size) spiral galaxies in HeViCS, among them NGC 4501.

2.3. The calibration of metallicity and the abundance gradients

The metallicity measurements of these galaxies are available in the literature from optical spectroscopy of their HII regions. The most direct method to derive the oxygen abundance is to measure the electron temperature (T_e) of the ionized gas using the intensity (relative to a hydrogen recombination line) of one or more temperature-sensitive auroral lines such as [O III] $\lambda 4363$ Å, [N II] λ 5755 Å, [S III] $\lambda 6312$ Å, and [O II] $\lambda 7325$ Å, as summarized by Moustakas et al. (2010). However, measurements of the electron temperature were not available from the spectroscopic observations in the original papers of McCall et al. (1985), Shields et al. (1991), Henry et al. (1994), and Skillman et al. (1996). The temperature diagnostic lines are indeed intrinsically faint in metal-rich HII regions. Therefore, oxygen abundance has been derived using the strong-line abundance calibrations which relate the metallicity to one or more line ratios involving the strongest recombination and forbidden lines. In particular, the oxygen excitation index $R_{23} = ([OII]+[OIII])/H_\beta$ is one of the most often adopted calibrators to estimate the nebular abundances. As discussed by Moustakas et al. (2010), the principal advantage of R_{23} as an oxygen abundance diagnostic is that it is directly proportional to both principal ionization states of oxygen, whereas one of the major disadvantages is that the relation between R_{23} and metallicity is degenerate for low and high metallicity.

However, the calibrations of the metallicity by means of the strong-line ratios are not unique. They can be divided in three main categories: those calibrated with photoionization models (e.g., McGaugh 1991; Zaritsky et al. 1994; Kewley & Dopita 2002; Kobulnicky & Kewley 2004); those calibrated directly with the electron temperature, called empirical methods (e.g., Pilyugin 2001; Pettini & Pagel 2004; Pilyugin & Thuan 2005); and those combining both methods (e.g., Denicoló et al. 2002). As discussed widely in Kewley & Ellison (2008), the abundances derived with different methods do not have a common absolute oxygen abundance scale. The oxygen abundances derived using the theoretical calibration are up to a factor of ~4 higher than those based on the empirical calibration. However, despite the significant zero-point offset in the abundance scales, to first order the slope of the abundance gradients agrees when calculated with different calibrators (see Moustakas et al. 2010).

We have tested the effect of several metallicity calibrators in NGC 4254, the galaxy with the best sampled metallicity gradient. Starting with the abundance estimates from Moustakas et al. (2010), based on literature spectroscopy calibrated with the Kobulnicky & Kewley (2004, hereafter KK04) formula, we used the relationships provided by Kewley & Ellison (2008) to convert to other abundance scales. The relationships of Kewley & Ellison (2008) are obtained for limited oxygen abundance ranges, corresponding to the ranges where they could perform
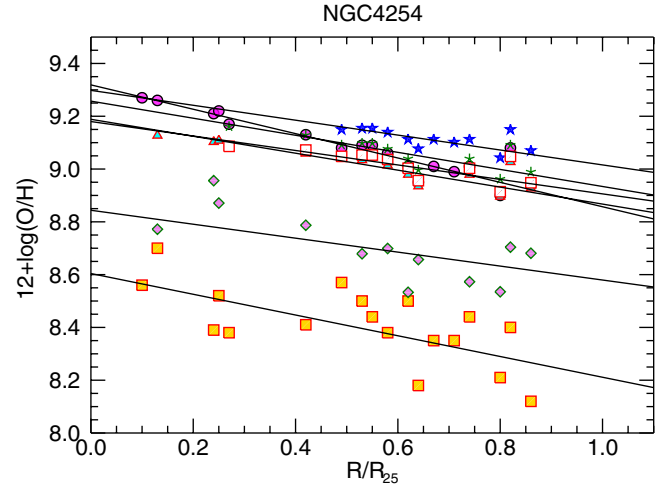

Fig. 1. The oxygen abundance gradient of NGC 4254 obtained with several metallicity calibrations: Kobulnicky & Kewley (2004) (magenta circles), Pilyugin & Thuan (2005) (yellow squares), Zaritsky et al. (1994) (cyan triangles), McGaugh (1991) (blue stars), Kewley & Dopita (2002) (empty squares), Tremonti et al. (2004) (green asterisks), and Pettini & Pagel (2004) (violet diamond).

a polynomial fit to transform one abundance scale to another. Because of this, from the abundances of KK04 we were unable to recover the oxygen determination of Pettini & Pagel (2004) and Pilyugin & Thuan (2005). For these cases, we recomputed the oxygen abundance from the original spectra (McCall et al. 1985; Shields et al. 1991; Henry et al. 1994).

In Fig. 1, we show the result of our test: while the slope of the gradient is almost invariant with different calibrations, the zero-point depends on the choice of the calibration. In Fig. 3 we show the radial variation of dust temperature. In particular, the empirical calibrations of Pettini & Pagel (2004) and Pilyugin & Thuan (2005) show values of the oxygen abundances roughly 0.5–0.8 dex lower than the other determinations. These two latter empirical calibrations were obtained for HII regions with available electron temperature in a relatively low metallicity regime. They could not be valid for metal rich environments, as the galaxies of our sample. In Sect. 4.1 we will discuss how the dust-to-gas ratio might help in setting a lower limit to the metallicity and to discriminate among different calibrations.

2.4. HI and CO maps

The radial profile of the gas, including both atomic and molecular components, is necessary to derive the dust-to-gas mass ratio gradient. For NGC 4254, NGC 4321, and NGC 4501, we use the moment-0 HI maps obtained with VLA Imaging survey of Virgo galaxies in Atomic gas (VIVA) survey by Chung et al. (2009a). VIVA observations reach a column density sensitivity of $3-5 \times 10^{19}$ cm^{-2}. The comparison of their total HI fluxes with values in the literature from single dish observations gives a good agreement especially for the large galaxies, indicating no loss of flux in the interferometric observations (see Fig. 5 in Chung et al. 2009a). The beam sizes are: 30″86 × 28″07 for NGC 4254, 15″90 × 14″66 for NGC 4321, and 16″83 × 16″41 for NGC 4501. The HI radial profile of NGC 4303 is available from Warmels (1988) and Cayatte et al. (1990). We adopt the combined radial profile of the two, shown in Fig. 3 of Skillman et al. (1996).

Maps of molecular gas were available thanks to the ^{12}CO ($J = 1-0$) mapping survey of 40 nearby spiral galaxies, performed with the Nobeyama 45 m telescope by Kuno et al. (2007).

3. Analysis

3.1. The mass and temperature of dust

Maps of the dust temperature and mass surface density were obtained as in Smith et al. (2010). The images of the galaxies from the five PACS (100 and 160 μm) and SPIRE (250, 350, and 500 μm) bands were all convolved and re-gridded to the lower resolution (*FWHM* = 36.''9, 3 kpc) and pixel size (14.''0, 1.1 kpc) of the 500 μm observations. We used only pixels with $S/N > 10$ at 500 μm (the rms of our maps in this band is about 0.3 MJy/sr, see Davies et al. 2011). The selection of these high surface-brightness pixels was necessary to limit the uncertainties due to background subtraction and avoid the artefacts caused by the high-pass filtering in the PACS data reduction. Despite this limit, we were able to study the dust and gas properties up to at least 0.7 R_{25}[1] in all galaxies. For each galaxy we thus considered approximately 150−200 pixels covering about 1/2 of the optically defined area.

We estimated the error on the surface brightness on a pixel by pixel basis by comparing galaxy images from the two scan data used in this paper with those relative to other two scans recently taken by *Herschel* which cover only part of the HeViCS field. We found errors very similar to those estimated on the total fluxes (see Davies et al. 2011). Including a calibration error of 15% for PACS (PACS ICC, priv. comm.) and 7% for SPIRE (SPIRE observer's manual, 2010), the total error is 30%, 20%, 10%, 10%, and 15% of the flux at 100, 160, 250, 350 and 500 μm, respectively.

The SED for each pixel was fitted with a single modified blackbody, using a power law dust emissivity $\kappa_\lambda = \kappa_0(\lambda_0/\lambda)^\beta$, with spectral index $\beta = 2$ and emissivity $\kappa_0 = 0.192$ m^2 kg^{-1} at $\lambda_0 = 350$ μm. These values reproduce the average emissivity of models of the Milky Way dust in the FIR-submm (Draine 2003). The fit was obtained with a standard χ^2 minimization technique. In the pipeline calibration, the flux density observed by the various instruments, i.e. weighted over each filter passband, is converted into a monochromatic flux density assuming $F_\nu \propto \nu^{-1}$. Before fitting a modified blackbody, a color correction should be applied to the data, to account for the real spectral slope of the source. Alternatively, the conversion implemented into the pipeline calibration can be removed from the data (in SPIRE parlance this is equivalent to dividing the pipeline flux densities by the K_4 factor; SPIRE observer's manual, 2010); the passband weighted flux thus obtained should then be compared with the mean of the model flux density over the spectral response function for each of the bands. We adopted this second technique, using the appropriate response functions for the PACS and SPIRE bands (for SPIRE, we used the response functions for extended emission). However, color corrections are small for the adopted emissivity and the temperature range derived here (see Davies et al. 2011).

In Fig. 2 we show typical SEDs and graybody fits for three positions of different dust temperature in NGC 4254. As shown by the figure, a single temperature modified blackbody with
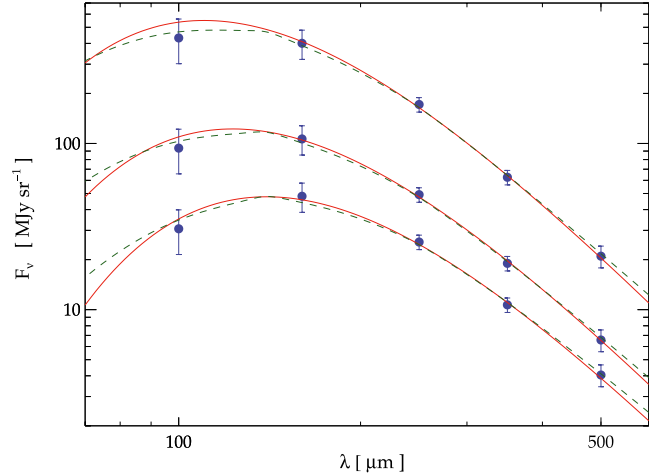

Fig. 2. Typical SEDs on three different positions (pixels) on NGC 4254. Blue dots are the measured (color-corrected) fluxes and the red (solid) + curves are the modified blackbody fits. The three SED correspond to minimum ($\approx$21 K), mean ($\approx$23.5 K), and maximum ($\approx$26 K) temperature in the galaxy (see Fig. 3). The green (dashed) curves show the fit of the Draine & Li (2007) model to the data, for IRSFs of intensities 2, 4 and 8 times the Local ISRF (see their paper for details).

$\beta = 2$ is sufficient to obtain reasonable fits of the SED over the wavelength range considered here (see also Davies et al. 2011). When data at shorter wavelength than PACS 100 μm is available, one might want to consider a two-component model, to include emission from warmer dust that might significantly contribute at least to the 100 μm flux. This is done, for example, by Bendo et al. (2010b), who used *Herschel* data, and by Smith et al. (2010) who used 70 μm data from the *Spitzer* satellite. However, they found that the inclusion of a warmer temperature component, thought necessary to fit the 70 μm data, improves the fit at $\lambda > 100$ μm only slightly, and does not modify significantly the estimate of the temperature and mass surface density of cold dust.

3.2. Sources of uncertainty in mass and temperature of dust

When only the errors on photometry are considered, the uncertainty in the determination of the temperature is about 2 K, and thus ~20% on the dust mass surface density.

In principle, fitting the dust SED with a single thermal-equilibrium temperature component could result in larger uncertainties in the dust mass estimates: grains of a given size and material could be exposed to different intensities of the interstellar radiation field (ISRF) and thus attain different equilibrium temperatures which will contribute differently to the SED; conversely, for the same radiation field the SED could depend on the dust distribution, because it results from the emission of a mixture of grains of different size and composition, each with its own equilibrium temperature. We found neither of these to have a strong effects on our mass estimates. In fact, by fitting the SED pixel by pixel, we already take into account the gradients due to the diffuse ISRF, which is more prominent in the radial direction than in the vertical directions (i.e. along the line of sight, for non edge-on disks; Bianchi et al. 2000).

However, the temperature radial gradients found here (see Sect. 3.3) would not produce very large uncertainties, even when the global SED is fitted with a single temperature model. For our targets, the differences between the sum of the dust mass in each pixel, and the dust mass obtained by fitting the sum of

---

[1] R_{25} is the radius of the galaxy measured to a B surface brightness of 25 mag arcsec^{-2}, and is an indication of the size of the galaxy; R_{25} were obtained from NED; ~0.7 R_{25} is equivalent to the solar radius in our Galaxy.

the flux densities in each pixel, is smaller than the fit error. The insensitivity of the global dust SED fitting on the shallow diffuse ISRF gradient is clearly shown in the analysis of the the FIR/submm SED of late type galaxies of Draine et al. (2007): though the more complex fitting procedure includes a dust grain model and a range of ISRF intensities (see also Draine & Li 2007), the global SED at $\lambda \geq 100\,\mu$m is found to be fitted by a dust component that accounts for most of the dust mass (a part from a few percents), heated by an IRSF of constant intensity.

We evaluated the effects of a complex dust mixture by fitting the model of Draine & Li (2007) to our pixel-by-pixel SED. Following Draine et al. (2007), we used a single value of the ISRF for emission at $\lambda \geq 100\,\mu$m. An example can be seen in Fig. 2. The SED from the dust grain mixtures and our single temperature model fit equally well the data. The dust mass obtained by using the procedure of Draine et al. (2007) is higher by about 10%, that is, within the error we quoted. Thus, the dust mass derived from a simple averaged emissivity, and a single IRSF – or temperature –, is not severely underestimated.

Larger uncertainties can come also from the assumption for the emissivity. For example, the value of the emissivity derived by James et al. (2002) from SCUBA observations of galaxies is equivalent to $\kappa_0 = 0.41$ m^2 kg^{-1}, a factor of two larger than the value we adopted. Adopting this emissivity would result in dust surface densities a factor of two smaller than what we found in this paper.

Also, dust emissivity has been reported to increase by about a factor two in grains associated to denser environments (see, e.g., Bianchi et al. 2003). However, this might be the case for extreme environments and not representative of the bulk of the diffuse dust mass: in the Milky Way, recent results from the Planck satellite show no emissivity variation between dust associated with HI and CO emission, nor emissivity variations with the galactocentric radius (Planck Collaboration et al. 2011). In Sect. 4.1 we will discuss how the uncertainty on κ_0 might affect our discussion.

The limited wavelength coverage does not allow us to investigate in details the effect of variation of the emissivity spectral index. In any case, the modified $\beta = 2$ blackbody provides good fits for all the SEDs analised here, as well as for the global SEDs in a larger sample of HeViCS objects (Davies et al. 2011). Local variations of the dust emissivity index with temperature, as those reported by Paradis et al. (2010) cannot be easily verified in our dataset. Variation of β from 1.7 to 2.2, as those measured at a reference temperature of 20 K, would result in an underestimate and overestimate of the dust mass of the same order as the quoted errors, respectively. Lower β values, as those found for dust at higher temperatures, will not be able to provide good fits to our SEDs in the central part of the galaxies.

Maps of the temperature and dust mass surface density for NGC 4501 have been presented in Smith et al. (2010). For the other galaxies, they will be presented in Vlahakis et al. (in prep.).

3.3. Radial profiles

The galaxies in our sample are disturbed by tidal interactions, thus we consider more reliable the determination of the geometric parameters of the galactic disks from kinematics rather than from photometry (see, for example, the discrepancy between parameters derived with the two methods for the case of NGC 4321 in Chung et al. 2009a). The task ROTCUR of the package NEMO (Teuben 1995) was used to fit a tilted ring model to the 21-cm moment-1 maps from the VIVA dataset. We
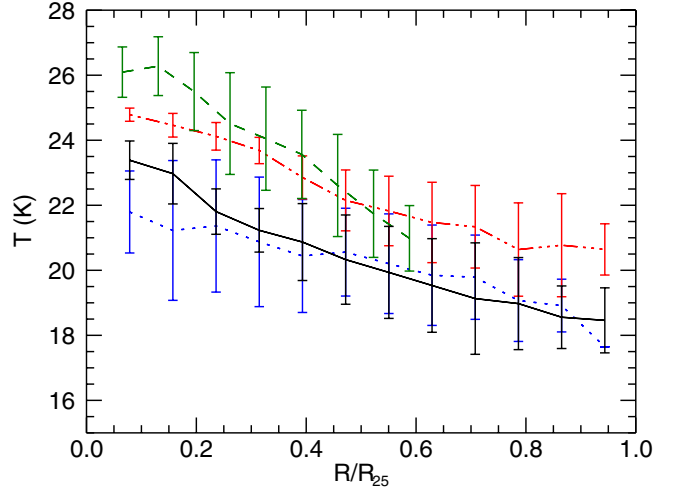

Fig. 3. Radial variation of dust temperature in NGC 4254 (red dotdashed curve), NGC 4303 (green dashed line), NGC 4321 (blue dotted curve), and NGC 4501 (black solid curve).

obtained values for the rotational velocity, the inclination and the position angle, as a function of the galactocentric radius.

The radial variations of i and PA are shown in Fig. 4. The average values are indicated with solid lines. For NGC 4321 and NGC 4501, i and PA are quite constant with radius and thus we use the average parameters in the whole radial range. For NGC 4254, which is a one-armed spiral, the variations of PA and i are important due to its asymmetric shape. Since in our comparison between metallicity and dust-to-gas mass ratio gradients we are interested mostly in the inner regions where the metallicity data are available, for NGC 4254 we used i and PA averaged in the regions with galactocentric radius $R_G < R_{25}$ (dashed line in Fig. 4, top panels) where the variations are small. Pohlen et al. (2010) also found different ellipse parameters for the outer parts and for the inner parts of NGC 4254. For NGC 4303, for which VIVA maps are not available, we adopted the parameters by Koda & Sofue (2006).

The final values are shown in Table 1: in Col. 1 we show the galaxy name, in Cols. 2 and 3 the mean i and PA, in Col. 4 the optical diameter D_{opt} in arcmin, in Cols. 6−8 the slope of the metallicity gradient, the metallicity at the equivalent solar radius $0.7\,R_{25}$, and their reference. For NGC 4254 we report the value we adopt, i.e. the average within the optical radius, and in square brackets the average in the whole radial range. Between square brackets, for all galaxies, we report also inclinations and position angles from the literature, which are generally in good agreement with our values in the radial range considered.

The atomic and molecular gas maps were convolved to the same resolution of the SPIRE 500 μm map and re-gridded on the same pixel scale. The radial bin size in the profiles correspond to 1 pixel in the maps (14″ corresponding to $\sim$1.1 kpc). Adopting the geometric parameters in Table 1, we used a dedicated IDL procedure to obtain radial profiles (azimuthally averaged over elliptical annuli) for HI, CO, and dust mass surface density. The profiles are shown in Figs. 5: the top panels contain PACS and SPIRE profiles at 100, 160, 250, 350, and 500 μm (from top to bottom) for NGC 4254, NGC 4303, NGC 4321, and NGC 4501; the bottom panels the profiles of dust (green), HI (red), and H$_2$ (blue) surface density, where the CO flux is converted into H$_2$ using the standard conversion factor $X_{CO} \approx (1.8 \pm 0.3) \times 10^{20}$ cm^{-2} (K km s^{-1})$^{-1}$ (see below). For all galaxies H$_2$ is dominant in the inner-most regions, while
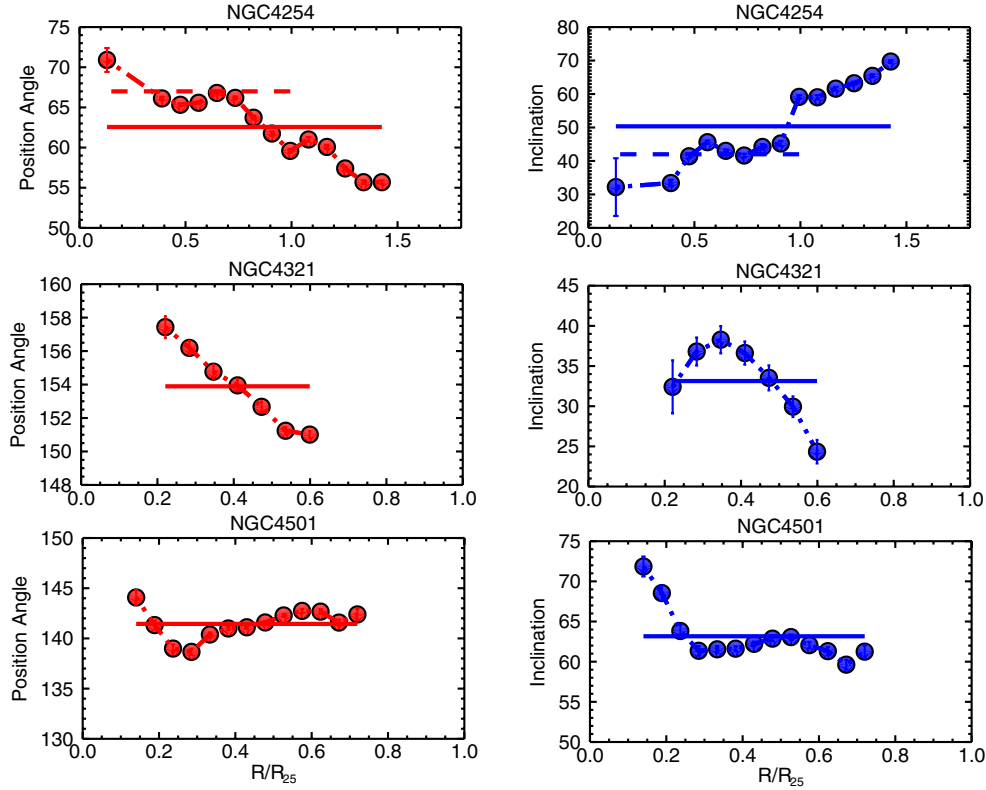
Fig. 4. Radial variation of position angle and inclination in NGC 4254, NGC 4321, and NGC 4501 from moment-1 H I maps. The continuous lines are the average in the whole radial range, whereas the dashed line is the average in the region $R_G < R_{opt}$ for NGC 4254.

Table 1. Parameters of the sample galaxies.

Name	Inclination	Position angle	$D_{opt}{}^a$ (arcmin)	Slope$_{KK04}$ (dex/R_{25})	$12 + \log(O/H)_{KK04}$ at $R_G = 0.7\,R_{25}$	Ref.
(1)	(2)	(3)	(4)	(5)	(6)	(7)
NGC 4254	42° (53°)[b] [42°][d]	67° (61.6°)[b] [68°][d]	5.6	−0.42 ± 0.06	8.84 ± 0.02	M10[c]
NGC 4303	30°[e]	135°[e]	6.5	−0.42 ± 0.02[‡]	9.24 ± 0.02	S96[c]
NGC 4321	33° [26°][f]	154.4°[155°][f]	7.6	−0.35 ± 0.13	9.04 ± 0.04	M10[c]
NGC 4501	63°[58°][g]	141.4°[140°][g]	7.1	−0.07 ± 0.16[‡]	9.30 ± 0.21	S96[c]

Notes. [a] D_{opt} is $2 \times R_{25}$; [b] average values for $R_G < R_{25}$ and, between brackets, throughout the whole radial range; [c] M10 = Moustakas et al. (2010) and S96 = Skillman et al. (1996); [d] Phookun et al. (1993); [e] Koda & Sofue (2006); [f] Canzian & Allen (1997); [g] Kenney & Young (1988). [‡] We recomputed the gradient slope of NGC 4303 and NGC 4501 using data from Skillman et al. (1996), converting them with Kewley & Ellison (2008) formula to the KK04 scale, obtaining different values with respect to those quoted in their paper.

HI becomes dominant over H$_2$ at $R > 0.5-0.6\,R_{25}$. HI radial profiles are quite flat within R_{25}, whereas both H$_2$ and dust profiles are decreasing with radius.

The errors on the radial profiles were estimated by a combination in quadrature of the uncertainty in the overall absolute calibration and of the standard deviation of the fluxes in each radial bin. Typical errors are of the order of 10−30%. However, uncertainties for the dust mass are mainly due to the choice of the model parameters and can vary by a factor two.

In the next section, we report the total mass of H$_2$ obtained with the different assumptions on X_{CO} (Table 4).

3.4. The X_{CO} factor

To convert ^{12}CO observation to measure the amount of molecular hydrogen we assume a CO-to-H$_2$ conversion factor

$$X_{CO} = N(H_2)/\int I(CO)\,dv$$

(Lebrun et al. 1983). In our Galaxy $X_{CO} \approx (1.8 \pm 0.3) \times 10^{20}$ cm^{-2} (K km s^{-1})$^{-1}$ with excursions of up to a factor of ~2 over this value, particularly at high latitudes (Dame et al. 2001). Shetty et al. (2011) and Leroy et al. (2009) showed that X_{CO} can vary even more, especially in low metallicity environments where it can reach $X_{CO} \sim 100 X_{Gal}$.

As derived by analysis of observations by Bolatto et al. (2008) and by theoretical models (Glover & Mac Low 2011), this factor can vary due to effects of abundance, excitation, optical depth, and cloud structure averaged over a large area. In particular, the abundance of the heavy elements has an important impact on the value of X_{CO} (Israel et al. 1986; Maloney & Black 1988). Metallicity affects cloud structure both directly, as smaller abundances of C and O translate into lower abundance of CO, and indirectly, as a lower dust-to-gas mass ratio diminishes the H$_2$ formation rates and the shielding of molecular gas from the photo-dissociation by ultraviolet radiation. As summarized by Bolatto et al. (2008), there are several observational
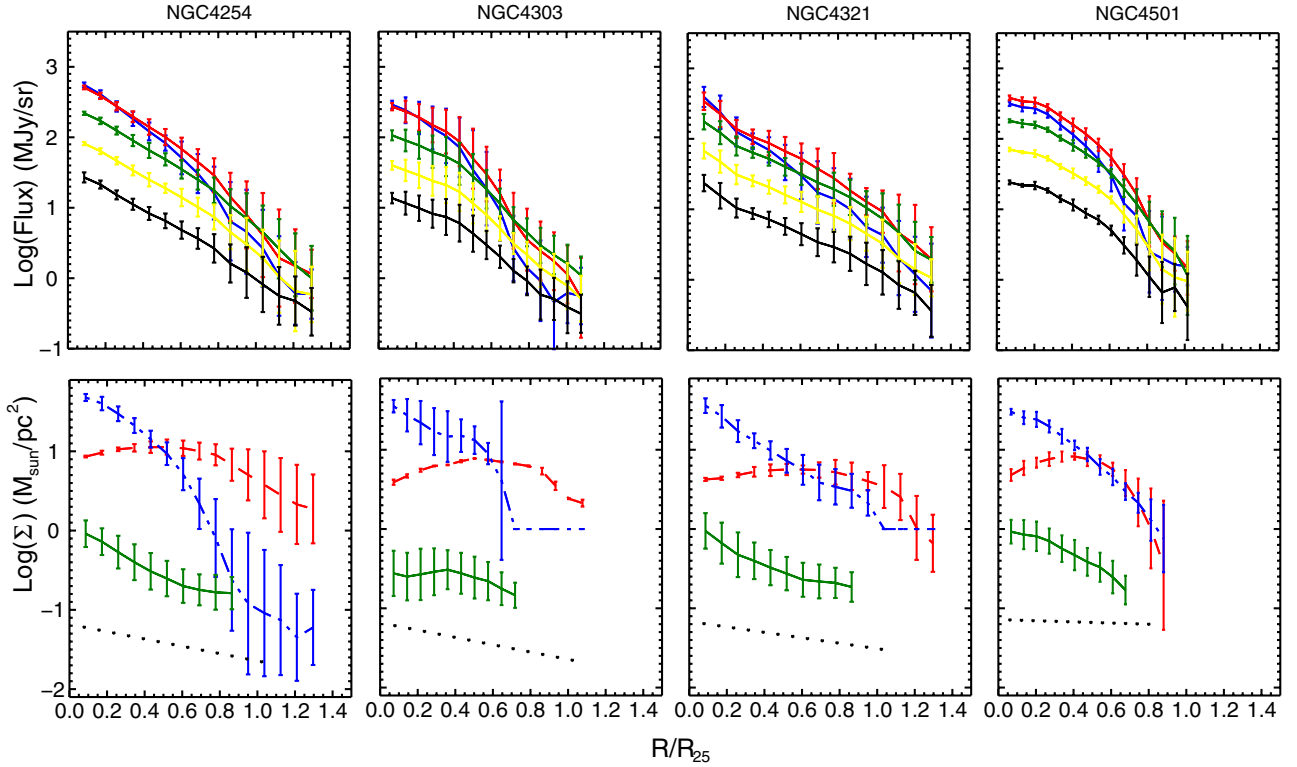
Fig. 5. *Top panels*: radial profiles of dust emission at 100, 160, 250, 350, 500 μm (*from top to bottom*) for NGC 4254, NGC 4303, NGC 4321, NGC 4501. *Bottom panels*: radial profiles of dust mass (green solid line), HI (red long dashed line), H_2 (blue dot-dashed line) surface density using a uniform conversion factor $X_{CO} \approx (1.8 \pm 0.3) \times 10^{20}$ cm^{-2}, and the O/H radial gradient (dotted line, scaled of a factor 10.5 to match the logarithmic scale of the other quantities).

calibrations of X_{CO} with the metallicity, Z, in the literature, showing a range of behaviors; most of the calibrations find an increasing X_{CO} with decreasing Z (e.g., Wilson 1995; Barone et al. 2000; Israel et al. 2003; Strong et al. 2004).

The dependence varies from $X_{CO} \sim Z^{-2.5}$ (Israel 2000) to $X_{CO} \sim Z^{-1}$ (Wilson 1995; Arimoto et al. 1996; Boselli et al. 2002), while Bolatto et al. (2008) do not find any measurable trend in the range from $8 < 12 + \log(O/H) < 8.8$ on the scales of the individual CO-bright giant molecular clouds, but they did not argue for a Galactic X_{CO} on large scales. Strong & Mattox (1996) also found a constant X_{CO} with metallicity. However, few works were dedicated to the metallicity dependence of X_{CO} in super-solar regions, as for example the study of Arimoto et al. (1996) who investigated X_{CO} also in two metal-rich galaxies, namely M 31 and M 51. The spiral galaxies in Virgo are thus of particular importance to verify the assumed dependence on metallicity of X_{CO} in metal-rich environments. To evaluate the conversion factor X_{CO} at different metallicities and relate it to the dust-to-gas ratio, we compared three different assumptions:

i) *Uniform*: we used the standard Galactic value from Bolatto et al. (2008) $X_{CO} \approx 1.8 \times 10^{20}$ cm^{-2} (K km s^{-1})$^{-1}$ (hereafter Galactic X_{CO}) throughout the radial range.
ii) *Linear metallicity dependence*: we used a linear metallicity dependence as found by Arimoto et al. (1996); Boselli et al. (2002). This is similar to the -0.67 slope derived by Wilson (1995). We adopted the analytic calibration given by Wilson (1995), but rely on the most recent oxygen solar abundance of Asplund et al. (2009) instead of Grevesse & Anders (1989). Assuming that at the new solar oxygen abundance,

$12 + \log(O/H) = 8.69$, $X_{CO} \approx 1.8 \times 10^{20}$ cm^{-2} (K km s^{-1})$^{-1}$, the Boselli et al. (2002)'s relationship becomes

$$\log(X_{CO}) = -1.0 \times (12 + \log(O/H)) + 8.94 \qquad (1)$$

where X_{CO} is expressed in unit of 10^{20} cm^{-2} (K km s^{-1})$^{-1}$.
iii) *Super-linear metallicity dependence*: we considered a super-linear dependence on metallicity as found by Israel (2000). Re-scaling to the Asplund et al. (2009) solar oxygen abundance, the Israel (2000) relationship becomes

$$\log(X_{CO}) = -2.5 \times (12 + \log(O/H)) + 21.72 \qquad (2)$$

where X_{CO} is again expressed in unit of 10^{20}.

4. The method

We started from the hypothesis that dust-to-gas mass ratio and O/H are tracing the same quantity, i.e. the metal abundance relative to hydrogen. Thus we expected that the slope of the two radial gradients agree. Within this hypothesis, we attempted to constrain the value of X_{CO}, and eventually its dependence on metallicity, using the information contained in the slope of the metallicity gradient. In fact, due to the large discrepancy on the zero-point of different calibrations as discussed by, e.g., Kewley & Ellison (2008), it is difficult to place these galaxies on an absolute metallicity scale using only inferences from HII optical spectroscopy.

Here we summarize the steps, while the details are given in the following sections.

I. We converted the dust-to-gas mass ratio in oxygen abundances with the relationship of Draine et al. (2007) (see

Eq. (3)), thus obtaining an approximate zero-point for the metallicity scale.

II. We computed the radial profile of the dust-to-gas mass ratio with the Galactic X_{CO}.

III. Once fixed the approximate abundance scale, we compared the radial profiles of the dust-to-gas mass ratio with the super-linear and linear metallicity dependences of X_{CO}.

4.1. I. The dust-to-gas ratio and metallicity scales

If we consider that the abundances of all heavy elements are proportional to the oxygen abundance and that all heavy elements condensed to form dust in the same way as in the MW, then the dust-to-gas mass ratio scales proportionally to the oxygen abundance (Draine et al. 2007)

$$\frac{M_{dust}}{M_H} \approx 0.007 \frac{(O/H)}{(O/H)_\odot}, \tag{3}$$

where 0.007 is the dust-to-hydrogen ratio of the MW at solar radius, $\sim 0.7 R_{25}$ with optical radius of our Galaxy of 12 kpc (Reshetnikov 2000). In Eq. (3), we use the observed dust-to-gas ratio 0.0073 estimated from observed depletions in the solar neighborhood instead of the value from dust models, 0.010, about 40% larger (Draine et al. 2007), and the solar oxygen abundance $12 + \log(O/H)_\odot = 8.69$ from Asplund et al. (2009).

A similar relationship was obtained also by Boselli et al. (2002) using the data available for the MW (Sodroski et al. 1994), the LMC (Koornneef 1982), and the SMC (Bouchet et al. 1985).

We converted the dust-to-gas ratio, obtained with the Galactic X_{CO} at $R_G = 0.7 R_{25}$, into $12 + \log(O/H)$ with Eq. (3).

Before comparing the metallicity derived from dust-to-gas ratio with that derived from nebular oxygen abundances, we estimated the effect of the assumed values of the mass emissivity coefficient and of the X_{CO} on the metallicity derived from Eq. (3). Because the determinations of the total gas mass take place in regions where H_2 is not negligible, the dust-to-gas ratio depends indeed critically on what is assumed about X_{CO}. First, we checked the value of the dust-to-gas ratio we would obtain at $R_G = 0.7 R_{25}$ adopting different X_{CO}: using $X_{CO} \approx 4 \times 10^{20}$ cm^{-2} (K km s^{-1})$^{-1}$ we would have a dust-to-gas ratio ~ 0.2 dex lower and using $X_{CO} \approx 0.5 \times 10^{20}$ cm^{-2} (K km s^{-1})$^{-1}$ we would obtain a dust-to-gas ratio ~ 0.2 dex higher. Thus an uncertainty of ± 0.2 dex is associated to the choice of X_{CO}.

Then, we verified how the emission coefficient could affect our discussion. In the most unfavorable conditions we could overestimate (or underestimate) the dust mass by a factor two, corresponding to a variation of O/H derived from Eq. (3) of ± 0.3 dex.

In addition, we have that a typical error on the dust-to-gas mass ratio of $\sim 30-50\%$ (including the flux calibration) translates into errors of $\sim 0.10-0.15$ dex in O/H. Considering that these sources of uncertainty are independent we combine them in quadrature, obtaining a total uncertainty of ~ 0.35 dex.

We compared with $12 + \log(O/H)$ obtained at the same galactocentric distance with three calibrations: KK04, Pettini & Pagel (2004, PP04), and Pilyugin & Thuan (2005, P05). The results for NGC 4254, NGC 4303, NGC 4321, and NGC 4501 are shown in Table 2.

From the comparison of the metallicity obtained for dust-to-gas ratio with several metallicity calibrations we found that the calibrations of Pilyugin & Thuan (2005) show the largest discrepancy with the metallicity derived from dust also if we

Table 2. Oxygen abundance from dust-to-gas mass ratio at 0.7 R_{25}.

Name	O/H$_{dust-to-gas}$ 0.7 R_{25}	O/H$_{KK04}$	O/H$_{PP04}$	O/H$_{P05}$
(1)	(2)	(3)	(4)	(5)
NGC 4254	8.84	8.95	8.65	8.35
NGC 4303	9.24	9.24	8.94	8.64
NGC 4321	9.04	9.10	8.80	8.40
NGC 4501	9.04	9.30	8.90	8.70

consider all possible sources of errors, i.e., uncertainty on the emission coefficient, X_{CO}, flux calibrations, and tend to give lower O/H values. The calibrations of KK04 and Pettini & Pagel (2004) are, on the other hand, both consistent within the errors (~ 0.35 dex O/H$_{dust-to-gas}$ and ~ 0.1 dex for O/H from nebular abundances) with our findings from the dust-to-gas ratio. We conclude that, at the equivalent solar radius (0.7 R_{25}), the four galaxies in analysis are more metal rich than the MW at the same radius (the solar oxygen abundance is 8.69), thus a perfect environment to test if any dependence of X_{CO} with the metallicity is in place at high metallicity.

Our result is only in apparent disagreement with Draine et al. (2007). Their relationship between dust-to-gas and metallicity is derived theoretically assuming that the interstellar abundances of all heavy elements were proportional to O/H, and their fraction scales as in the MW, and then it is compared with the oxygen abundances obtained with the calibration of Pilyugin & Thuan (2005) and the dust-to-gas mass ratio adopting $X_{CO} \approx 4 \times 10^{20}$ cm^{-2} (K km s^{-1})$^{-1}$. They found a good agreement with the theoretical relationship within a factor of 2. In our analysis we found a better agreement with KK04 oxygen abundances since we are using a different X_{CO} factor and a different value of dust-to-gas in the MW at solar radius: the P05 oxygen abundances are indeed on average $2-4$ times lower than the KK04's ones, but this is compensated by a X_{CO} factor two times higher, and the assumed dust-to-gas in the MW for the dust models, ~ 1.5 higher than the one we used, which comes from observations.

With our choice of a Galactic $X_{CO} \approx 1.8 \times 10^{20}$ cm^{-2} (K km s^{-1})$^{-1}$, a dust-to-gas ratio in the solar neighborhood of 0.0073, and the relation in Eq. (3), we selected the metallicity scale of KK04, which best agrees with the scale derived from the dust-to-gas ratio, and convert the abundances of our galaxies to a common scale. For NGC 4254 and NGC 4321 we used the abundance determined by Moustakas et al. (2010) (based on literature spectroscopy calibrated with the formula of Kobulnicky & Kewley 2004). For NGC 4303 and NGC 4501 we used the original spectroscopy to calculate oxygen abundance on the abundance scale of KK04.

With the calibration of KK04, the abundances at 0.7 R_{25} are all super-solar ranging from ~ 8.95 to ~ 9.3, as shown in Table 2. The central oxygen abundances would range from 9.3 to 9.5, but we have to consider that they are an extrapolation of the metallicity gradient up to the galaxy centre and not a real measurement. In addition, the galaxy disk does not extend up to the central regions where the bulge is present. These central abundances are comparable with recent results obtained from direct electron temperature measurement in the HII regions of M 81, where the extrapolation of the metallicity gradient up to the galactic centre gives an oxygen abundance of 9.37 (Stanghellini et al. 2010), and in our Galaxy where the central O/H from the gradient of Rudolph et al. (2006) is 9.2 (determination of O/H with optical spectroscopy).
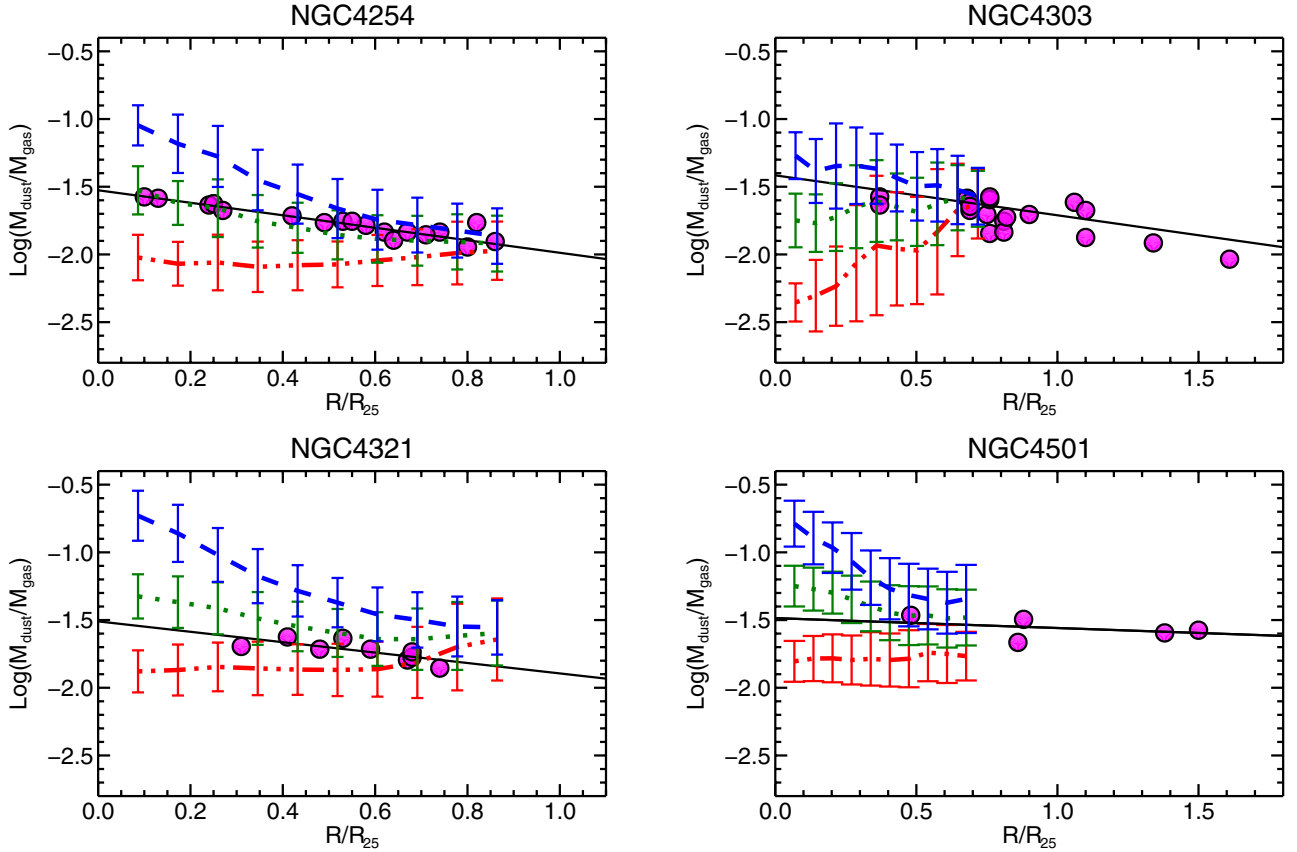
Fig. 6. Dust-to-gas mass ratio and metallicity radial profiles of NGC 4254, NGC 4303, NGC 4321, and NGC 4501 with the oxygen abundance calibrated with KK04. The conversion factors X_{CO} are: with the Galactic conversion factor (dot-dashed red curve), with the linear metallicity dependence as in Eq. (1) (dotted green curve), with the superlinear dependence on metallicity as in Eq. (2) (dashed blue curve). The magenta circles are the oxygen abundance converted to the dust-to-gas scale with Eq. (3). For NGC 4254 and NGC 4321 we used the recalculation by Moustakas et al. (2010), for NGC 4303 and NGC 4501 the oxygen abundances by Skillman et al. (1996) converted to the KK04 scale. The continuous black lines show the fit to the abundance data.

4.2. II. The dust-to-gas mass gradient with a standard X_{CO}

In Fig. 6 we show the comparison between the dust-to-gas mass ratio gradients, calculated with the Galactic conversion factor (red curves), and the oxygen abundance gradients (magenta circles and solid black lines) calibrated with KK04 and converted in the dust-to-gas mass scale with the relationship discussed in Sect. 4.1.

If we consider a constant Galactic X_{CO}, the slopes of the dust-to-gas and metallicity gradients are only in marginal agreement. In particular, the dust-to-gas gradients are flatter, with a slight positive slope at large galactocentric radii $R_G > 0.7 R_{25}$. For NGC 4254 and NGC 4321 the comparison between the metallicity and dust-to-gas mass ratio gradients is straightforward because their metallicity gradients are well determined in the same radial regions where the dust-to-gas map is obtained (Fig. 6, left panels). For NGC 4254 and NGC 4321 the dust-to-gas mass ratio gradient are flatter than the metallicity radial distribution, and they are constant within the errors, with a slightly increasing behaviour in the outer regions. The same is true also for NGC 4501, while for NGC 4303 dust-to-gas mass ratio gradient is positive. For these two galaxies we are planning new spectroscopic observations of HII regions in the inner regions to have a better overlap between dust-to-gas and metallicity.

4.3. III. Can we constrain X_{CO}?

We used Eqs. (1) and (2) along with the abundance gradients given in Table 1 to calculate the molecular gas surface densities, and then the dust-to-gas mass ratios.

The constant Galactic value of X_{CO} (dot-dashed red curves in Fig. 6) produces in most cases flat dust-to-gas mass ratio as discussed in Sect. 4.2. The super-linear dependence (dashed blue curves) results in a dust-to-gas radial gradient much steeper than the oxygen gradient, especially in the inner regions. A linear fit of the gradient in the logarithm of the dust-to-gas ratio [dlog(dust/gas)/dR_G] (Table 3) suggests that, within ~0.7 R_{25}, the linear metallicity dependence is able to reproduce, within the errors, the same radial slope of the metallicity gradient for NGC 4254 and NGC 4321. A flattening of the dust-to-gas mass ratio gradient is appreciable in the outer regions, where the HI component is dominant. For NGC 4303 a super-linear metallicity dependence of X_{CO} is instead necessary to match within the errors the two gradients. For NGC 4501 an X_{CO} value between the Galactic one and the one derived from the linear metallicity dependence is required.

From Fig. 5 we can figure out what is happening: for a fixed Galactic X_{CO} the dust-to-gas ratio would be constant, as in shown by dot-dashed red curves in Fig. 6. Once a metallicity dependence of the type described in Eqs. (1) and (2) is introduced in X_{CO}, that depresses the H$_2$ in the centers (which have

Table 3. Slopes of the O/H and dust-to-gas gradients within $0.7\,R_{25}$.

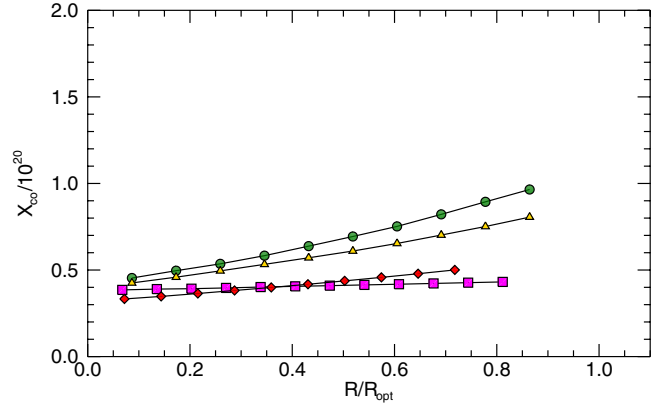| Name (1)	Slope$_{\rm O/H}$ (2)	Slope$_{\rm Gal}$ (3)	Slope$_{\rm linear}$ (4)	Slope$_{\rm superlinear}$ (5)
NGC 4254	-0.42 ± 0.06	0.07 ± 0.06	-0.55 ± 0.07	-1.17 ± 0.06
NGC 4303	-0.42 ± 0.02	1.11 ± 0.15	0.27 ± 0.13	-0.44 ± 0.11
NGC 4321	-0.35 ± 0.13	0.09 ± 0.09	-0.52 ± 0.08	-1.13 ± 0.09
NGC 4501	-0.07 ± 0.16	0.07 ± 0.07	-0.45 ± 0.07	-1.18 ± 0.12

Fig. 7. Radial variation of $X_{\rm CO}$ in the four galaxies with the metallicity computed with the calibration KK04 and the dependence in Eq. (1): NGC 4254 (green circles), NGC 4303 (red diamonds), NGC 4321 (yellow triangles), and NGC 4501 (magenta squares).

super-solar metallicity) and makes the total gas to look more like the atomic component, which generally has a much more constant distribution with $R_{\rm G}$ than the dust. Hence, when adopting the metallicity dependences of $X_{\rm CO}$, we favor the outwardly decreasing gradients in dust-to-gas ratio.

Given that these galaxies are dominated by the molecular gas component in their central regions, one could think that the result we found is, in a certain sense, expected: we use a $X_{\rm CO}$ that depends on $1/Z$ and we obtain a dust-to-gas mass ratio decreasing as Z. However, the radial dependence of $X_{\rm CO}$ has only a secondary impact on our results: to obtain a decreasing dust-to-gas mass ratio it is necessary only to have a conversion factor of the order of $\sim 1/3-1/2$ the Galactic value in the central regions of the galaxies, while the outer regions, where the atomic gas components is dominant, are less affected by the choice of $X_{\rm CO}$. From Fig. 7 where we show the radial dependence of $X_{\rm CO}$ obtained with Eq. (1) (linear dependence) for NGC 4254 (green circles), NGC 4321 (yellow triangles), NGC 4303 (red diamonds), and NGC 4501 (magenta squares), it can be seen that no larger radial variations of $X_{\rm CO}$ are required. To reproduce a decreasing dust-to-gas mass ratio gradient in the radial regions where the molecular gas dominates the gaseous component, we need for the sample galaxies an $X_{\rm CO} \sim 1/3$ of the Galactic value, slightly increasing with radius up to $\sim 2/3$ the Galactic value. These results agree with $X_{\rm CO}$ obtained in the metal rich HII regions of M 31 and M 51 (e.g., Arimoto et al. 1996).

To check this, we have used a constant $X_{\rm CO}$: 0.5×10^{20} cm^{-2} (K km s^{-1})$^{-1}$ for NGC 4254, 0.1×10^{20} for NGC 4303, 0.9×10^{20} for NGC 4321, and 0.7×10^{20} for NGC 4501. These values are chosen to produce the best agreement between O/H and dust-to-gas gradients for each galaxy of our sample. They are not related to the $X_{\rm CO}$ values derived from the metallicity dependence in Eq. (1) and shown in Fig. 7. Note that the case of NGC 4303 seems to be quite extreme: the $X_{\rm CO}$ necessary to reproduce with the dust-to-gas ratio the behaviour of the O/H gradient is much smaller than $1/3$ Galactic $X_{\rm CO}$, being 0.1×10^{20}.

We have compared these gradients also with the dust-to-gas mass ratio computed with constant "Galactic" $X_{\rm CO} = 1.8 \times 10^{20}$ cm^{-2} (Bolatto et al. 2008) and $X_{\rm CO} = 4.0 \times 10^{20}$ cm^{-2} (Draine et al. 2007). The results are shown in Fig. 8: with a lower $X_{\rm CO}$, the negative slope of the metallicity gradient is reproduced by the dust-to-gas mass ratio gradient. We note also that the outer regions are marginally affected by the choice of $X_{\rm CO}$, and they are still consistent with a "standard" $X_{\rm CO}$ values for normal disk galaxies, while the inner regions need a lower value to reproduce a decreasing dust-to-gas mass ratio. This is in agreement with the evidence found for a lower $X_{\rm CO}$ in galaxy centers, e.g., Sodroski et al. (1994), Israel et al. (2006), Israel (2009), Watanabe et al. (2011). On the other hand, the dust-to-gas mass ratio obtained with $X_{\rm CO} = 1.8 \times 10^{20}$ cm^{-2} and $X_{\rm CO} = 4.0 \times 10^{20}$ cm^{-2} tend to be flatter or positive, especially with the larger value of $X_{\rm CO}$. Thus, even if it is difficult to prove a dependence of $X_{\rm CO}$ on the metallicity due to uncertainties on the O/H and dust mass scales,

the comparison between the oxygen and dust-to-mass mass ratio radial gradients in the four galaxies under analysis allows us to put a constraint on their $X_{\rm CO}$ conversion factors, favoring lower values of $X_{\rm CO}$ in the radial regions $R_{\rm G} < 0.6-0.7\,R_{25}$.

In Table 4 we report the total masses of HI, H$_2$, and dust. We computed the dust masses integrating the radial profile up to $0.7\,R_{25}$. We remind that this limit is due to the requirement of a $S/N > 10$ at $500\,\mu$m, necessary to limit the uncertainties due to background subtraction and avoid the artefacts caused by the high-pass filtering in the PACS data reduction. The comparison with the results of Davies et al. (2011), obtained with an integrated analysis of the galaxies, indicates that only 30% of the dust mass resides in the outer-most regions, with $R > R_{25}$.

4.3.1. Comparison with other works

Bendo et al. (2010a) performed a similar analysis on NGC 2403, a late-type galaxy with a relatively low molecular fraction. Because in NGC 2403 the atomic gas is the largest component of the ISM, differing assumptions about $X_{\rm CO}$ (they used a constant value and a metallicity dependence as in our Eq. (2)) have only a minor impact on the radial profile of the dust-to-gas mass ratio. Unlike NGC 2403, in the galaxies of our sample the molecular gas dominates the ISM within $\sim 0.5\,R_{25}$, and thus a variation of $X_{\rm CO}$ has a significant effect on the dust-to-gas ratio. Bendo et al. (2010a) found with both the constant and metallicity dependent $X_{\rm CO}$ a good agreement between the O/H gradient (-0.084 ± 0.009 dex kpc^{-1}) and the dust-to-gas gradient (-0.093 ± 0.002 dex kpc^{-1}), with the dust-to-gas slope slightly steeper. They explain that variations in the ratio of oxygen to the other constituents of dust might originate the difference in the gradients. For example, carbon and oxygen are both produced by supernovae, but carbon is also generated by the nucleosynthesis of low and intermediate mass stars; thus C/O is expected to vary radially, as shown by Garnett et al. (1999).

Thomas et al. (2004) obtained a similar result in their study of the radial distribution of dust and gas in several nearby galaxies for which they had neutral hydrogen and 850 μm images available: their radial profiles of dust-to-gas mass ratio were flatter than the oxygen abundance gradients from HII regions. However in their galaxies CO observations were not available, so they were neglecting an important potentially dominant component in the inner regions.
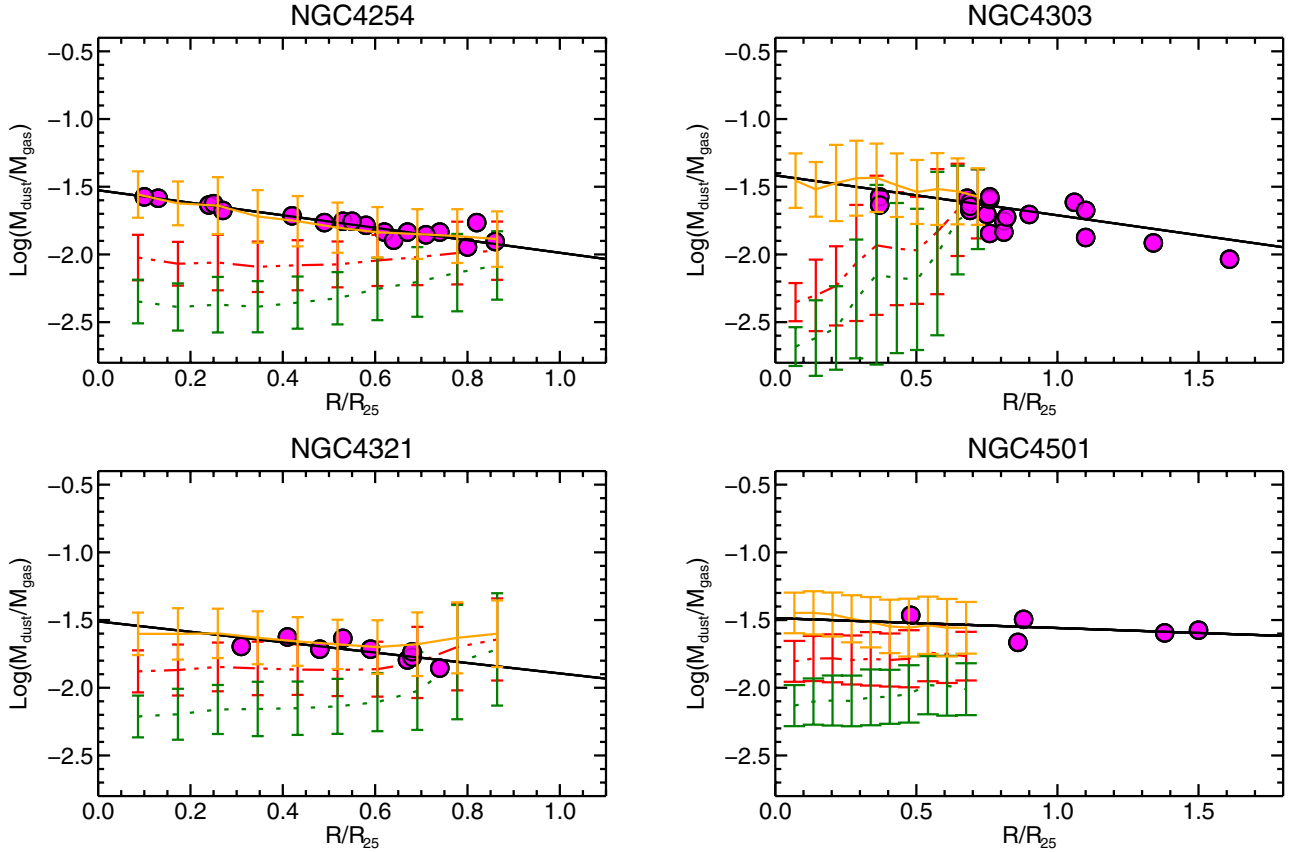
Fig. 8. Dust-to-gas mass ratio and metallicity radial profiles with the conversion factor X_{CO} $0.1-0.9 \times 10^{20}$ cm^{-2} (K km s^{-1})$^{-1}$ (see text for the X_{CO} adopted for each galaxy-orange solid curves), and with constant $X_{CO} = 1.8 \times 10^{20}$ cm^{-2} (red dot-dashed curves) and $X_{CO} = 4.0 \times 10^{20}$ cm^{-2} (green dotted curves). The magenta circles are the oxygen abundance converted to the dust-to-gas scale with Eq. (3). The continuous black lines show the fit to the abundance data.

Table 4. HI, H$_2$, and dust masses.

Name	M(HI) $10^9 M_\odot$	M(H$_2$)$_{unif.}$ $10^9 M_\odot$	M(H$_2$)$_{linear}$ $10^9 M_\odot$	M(H$_2$)$_{superlinear}$ $10^9 M_\odot$	M(dust) $10^7 M_\odot$
(1)	(2)	(3)	(4)	(5)	(6)
NGC 4254	4.4[a]	5.4	1.8	0.22	7.0
NGC 4321	4.8[a]	4.4	1.3	0.13	8.6
NGC 4303	3.3[b]	4.8	0.8	0.06	5.1
NGC 4501	2.7[a]	3.8	1.0	0.05	7.4

Notes. [a] Chung et al. (2009a); [b] integration of the radial profile shown in Fig. 3 of Skillman et al. (1996).

A similar result was obtained also by Muñoz-Mateos et al. (2009) in the galaxies belonging to the SINGS sample. They have studied the radial variation of the dust-to-gas ratio in a large sample of galaxies of different morphological types. They found that the dust-to-gas mass ratio decreases by an order of magnitude from the center to the edge of the optical disk of each galaxy, similarly to what happens for the gas-phase oxygen abundance. Their relation between dust-to-gas mass ratio and oxygen abundance can be described with a linear scaling law for $12 + \log(O/H) > 8.9$, as we found for NGC 4254, NGC 4321, and NGC 4501. At lower metallicities, they found that the dust-to-gas ratios are systematically below this simple relation. They explain this fact to be due to the large amounts of gas that has not yet undergone star formation activity and that reside in the outer regions of spiral disks.

4.4. Other evidence for a low X_{CO}

In agreement with our result, a value of X_{CO} lower than $\sim 2 \times 10^{20}$ cm^{-2} (K km s^{-1})$^{-1}$ was also expected in NGC 4254 and NGC 4321 from the analysis of Eales et al. (2010). They calibrated the mass-opacity coefficient (κ_ν) using their dust-to-gas maps. Using a standard X_{CO} value they found a mass-opacity coefficient significantly lower than the value (0.41 m^2 kg^{-1}) obtained by James et al. (2002). To solve the discrepancy, they suggested that using only SPIRE bands they are over-estimating the temperature of the dust; if the temperature of the dust in both NGC 4254 and NGC 4321 were actually $\simeq$10 K rather than 20 K, this would be enough to increase the value of κ_ν to that expected from the James et al. study. However, this is not the case since with our fit of PACS and SPIRE bands we found dust

temperatures in the range $17 < T < 25$ K found by Eales et al. (2010) (see Fig. 3).

The other possibility they suggested to reconcile their results with James et al. (2002) was to have values of $X_{CO} \simeq 6$ times lower than the initial value they assumed, about 2×10^{20} cm^{-2} (K km s^{-1})$^{-1}$. Considering that we are using a mass-opacity coefficient which is about half of that used by James et al., thus, to have agreement with our results, they would need $X_{CO} \simeq 3$ times lower than their standard value. This is consistent with our result; values of X_{CO} in the range about $0.5-1 \times 10^{20}$ cm^{-2} (K km s^{-1})$^{-1}$ can reproduce both the correct value of the mass-opacity coefficient and the radial profiles of dust-to-gas mass ratio.

5. Summary and conclusions

1. We analyzed FIR observations obtained with PACS and SPIRE, together with CO and HI maps from the literature, of four spiral galaxies in the Virgo cluster (NGC 4254, NGC 4303, NGC 4321, and NGC 4501). We derived the total mass of dust from SED fitting of the FIR images, and used HI moment-1 maps to derive the geometric parameters of the galaxies, which are disturbed by tidal interactions. Finally, we extracted the radial profiles of atomic gas, molecular gas and dust, and compare them with oxygen abundance radial gradients compiled from the literature and placed on a common abundance scale.

2. To avoid the large uncertainties on the zero-points of the oxygen abundance derived with the bright-line methods, we used the dust-to-gas ratio obtained with the Galactic value of X_{CO} to fix a lower limit to the oxygen abundance. This allowed us to discard a set of metallicity calibrations and to reduce the uncertainty on the oxygen gradient zero-point. We converted the literature O/H to the scale of KK04.

3. We studied the dependence of X_{CO} on metallicity by comparing the radial gradient of metal abundance in gas phase (oxygen abundance in HII regions) and in solid phase (dust in emission from the FIR versus the total gas-atomic and molecular), assuming that these two quantities decrease at the same rate with radius. We considered a constant X_{CO} (e.g., Bolatto et al. 2008), $X_{CO} \propto Z^{-1}$ ("linear" dependence) (e.g., Boselli et al. 2002), and $X_{CO} \propto Z^{-2.5}$ ("super-linear" dependence) (e.g., Israel 2000). A linear fit of the gradient in the logarithm of the dust-to-gas ratio [dlog(dust/gas)/dR_G] shows that, within ~ 0.7 R_{25}, values of X_{CO} in the range $\sim 0.5-0.9 \times 10^{20}$ cm^{-2} (K km s^{-1})$^{-1}$ were able to reproduce negative gradients, similar to the O/H ones for NGC 4254, NGC 4321, and NGC 4501, while NGC 4303 needs an extremely low X_{CO} value $\sim 0.1 \times 10^{20}$ cm^{-2} (K km s^{-1})$^{-1}$. For NGC 4254, these X_{CO} values can be obtained with a linear metallicity dependence and oxygen abundance calibrated by KK04. For NGC 4303 a superlinear dependence is instead necessary to match within the errors the two gradients, while for NGC 4501 and NGC 4321 a X_{CO} intermediate between the Galactic one and the linear metallicity dependence would be necessary (always with KK04 O/H calibration). We suggest that a X_{CO} lower than the standard Galactic one (e.g., Bolatto et al. 2008) is necessary in these galaxies to obtain a decreasing dust-to-gas mass ratio similar to the O/H gradient of HII regions. These low X_{CO} values are favored in the radial regions $R_G < 0.6-0.7$ R_{25} where the molecular gas dominates, while the outer regions, where the atomic gas is the main component, are less affected by the choice of X_{CO}, and thus we cannot put constraints on its value. A large sample of galaxies with available metallicity ad dust-to-gas mass ratio gradients is necessary to confirm and strengthen these results.

References

Arimoto, N., Sofue, Y., & Tsujimoto, T. 1996, PASJ, 48, 275
Asplund, M., Grevesse, N., Sauval, A. J., & Scott, P. 2009, ARA&A, 47, 481
Barone, L. T., Heithausen, A., Hüttemeister, S., Fritz, T., & Klein, U. 2000, MNRAS, 317, 649
Bendo, G. J., Wilson, C. D., Warren, B. E., et al. 2010a, MNRAS, 402, 1409
Bendo, G. J., Wilson, C. D., Pohlen, M., et al. 2010b, A&A, 518, L65
Bianchi, S., Davies, J. I., & Alton, P. B. 2000, A&A, 359, 65
Bianchi, S., Gonçalves, J., Albrecht, M., et al. 2003, A&A, 399, L43
Binggeli, B., Sandage, A., & Tammann, G. A. 1985, AJ, 90, 1681
Boissier, S., Boselli, A., Buat, V., Donas, J., & Milliard, B. 2004, A&A, 424, 465
Boissier, S., Gil de Paz, A., Madore, B. F., et al. 2005, ApJ, 619, L83
Bolatto, A. D., Leroy, A. K., Rosolowsky, E., Walter, F., & Blitz, L. 2008, ApJ, 686, 948
Boselli, A., & Gavazzi, G. 2006, PASP, 118, 517
Boselli, A., Lequeux, J., & Gavazzi, G. 2002, A&A, 384, 33
Boselli, A., Eales, S., Cortese, L., et al. 2010, PASP, 122, 261
Bouchet, P., Lequeux, J., Maurice, E., Prevot, L., & Prevot-Burnichon, M. L. 1985, A&A, 149, 330
Canzian, B., & Allen, R. J. 1997, ApJ, 479, 723
Cayatte, V., van Gorkom, J. H., Balkowski, C., & Kotanyi, C. 1990, AJ, 100, 604
Chung, A., van Gorkom, J. H., Kenney, J. D. P., Crowl, H., & Vollmer, B. 2009a, AJ, 138, 1741
Chung, E. J., Rhee, M.-H., Kim, H., et al. 2009b, ApJS, 184, 199
Dame, T. M., Hartmann, D., & Thaddeus, P. 2001, ApJ, 547, 792
Davies, J. I., Baes, M., Bendo, G. J., et al. 2010, A&A, 518, L48
Davies, J. I., et al. 2011, MNRAS, in press,
    DOI: 10.1111/j.1365-2966.2011.19993.x (Paper VIII)
Denicoló, G., Terlevich, R., & Terlevich, E. 2002, MNRAS, 330, 69
Draine, B. T. 2003, ARA&A, 41, 241
Draine, B. T., & Li, A. 2007, ApJ, 657, 810
Draine, B. T., Dale, D. A., Bendo, G., et al. 2007, ApJ, 663, 866
Dwek, E. 1998, ApJ, 501, 643
Eales, S. A., Smith, M. W. L., Wilson, C. D., et al. 2010, A&A, 518, L62
Garnett, D. R., Shields, G. A., Peimbert, M., et al. 1999, ApJ, 513, 168
Gavazzi, G., Boselli, A., Scodeggio, M., Pierini, D., & Belsole, E. 1999, MNRAS, 304, 595
Glover, S. C. O., & Mac Low, M.-M. 2011, MNRAS, 110
Griffin, M. J., Abergel, A., Abreu, A., et al. 2010, A&A, 518, L3
Grevesse, N., & Anders, E. 1989, Cosmic Abundances of Matter, 183, 1
Henry, R. B. C., Pagel, B. E. J., & Chincarini, G. L. 1994, MNRAS, 266, 421
Hirashita, H., Kaneda, H., Onaka, T., & Suzuki, T. 2008, PASJ, 60, 477
Inoue, A. K. 2003, PASJ, 55, 901
Israel, F. 2000, Molecular Hydrogen in Space, 293
Israel, F. P. 2009, A&A, 506, 689
Israel, F. P., de Graauw, T., van de Stadt, H., & de Vries, C. P. 1986, ApJ, 303, 186
Israel, F. P., Baas, F., Rudy, R. J., Skillman, E. D., & Woodward, C. E. 2003, A&A, 397, 87
Israel, F. P., Tilanus, R. P. J., & Baas, F. 2006, A&A, 445, 907
Issa, M. R., MacLaren, I., & Wolfendale, A. W. 1990, A&A, 236, 237
James, A., Dunne, L., Eales, S., & Edmunds, M. G. 2002, MNRAS, 335, 753
Kenney, J. D., & Young, J. S. 1988, ApJS, 66, 261
Kennicutt, R. C., Jr., Armus, L., Bendo, G., et al. 2003, PASP, 115, 928
Kewley, L. J., & Dopita, M. A. 2002, ApJS, 142, 35
Kewley, L. J., & Ellison, S. L. 2008, ApJ, 681, 1183
Kobulnicky, H. A., & Kewley, L. J. 2004, ApJ, 617, 240, KK04
Koda, J., & Sofue, Y. 2006, PASJ, 58, 299
Koornneef, J. 1982, A&A, 107, 247

Kuno, N., Sato, N., Nakanishi, H., et al. 2007, PASJ, 59, 117
Lebrun, F., Bennett, K., Bignami, G. F., et al. 1983, ApJ, 274, 231
Leroy, A. K., Bolatto, A., Bot, C., et al. 2009, ApJ, 702, 352
Lisenfeld, U., & Ferrara, A. 1998, ApJ, 496, 145
Maloney, P., & Black, J. H. 1988, ApJ, 325, 389
McCall, M. L., Rybski, P. M., & Shields, G. A. 1985, ApJS, 57, 1
McGaugh, S. S. 1991, ApJ, 380, 140
Moustakas, J., Kennicutt, R. C., Jr., Tremonti, C. A., et al. 2010, ApJS, 190, 233
Muñoz-Mateos, J. C., Gil de Paz, A., Boissier, S., et al. 2009, ApJ, 701, 1965
Paradis, D., Veneziani, M., Noriega-Crespo, A., et al. 2010, A&A, 520, L8
Pettini, M., & Pagel, B. E. J. 2004, MNRAS, 348, L59
Phookun, B., Vogel, S. N., & Mundy, L. G. 1993, ApJ, 418, 113
Pilbratt, G. L., Riedinger, J. R., Passvogel, T., et al. 2010, A&A, 518, L1
Pilyugin, L. S. 2001, A&A, 374, 412
Pilyugin, L. S., & Thuan, T. X. 2005, ApJ, 631, 231
Planck Collaboration, Abergel, A., Ade, P. A. R., Aghanim, N., et al. 2011, A&A, 536, A21 DOI: 10.1051/0004-6361/201116455
Poglitsch, A., Waelkens, C., Geis, N., et al. 2010, A&A, 518, L2
Pohlen, M., Cortese, L., Smith, M. W. L., et al. 2010, A&A, 518, L72
Reshetnikov, V. P. 2000, Astrophys., 43, 145
Roman-Duval, J., Israel, F. P., Bolatto, A., et al. 2010, A&A, 518, L74
Rudolph, A. L., Fich, M., Bell, G. R., et al. 2006, ApJS, 162, 346

Rupke, D. S. N., Kewley, L. J., & Chien, L.-H. 2010, ApJ, 723, 1255
Sauvage, M., Sacchi, N., Bendo, G. J., et al. 2010, A&A, 518, L64
Shetty, R., Glover, S. C., Dullemond, C. P., & Klessen, R. S. 2011, MNRAS, 11
Shields, G. A., Skillman, E. D., & Kennicutt, R. C., Jr. 1991, ApJ, 371, 82
Skillman, E. D., Kennicutt, R. C., Jr., Shields, G. A., & Zaritsky, D. 1996, ApJ, 462, 147
Smith, M. W. L., Vlahakis, C., Baes, M., et al. 2010, A&A, 518, L51
Sodroski, T. J., Bennett, C., Boggess, N., et al. 1994, ApJ, 428, 638
Sofue, Y., Koda, J., Nakanishi, H., & Hidaka, M. 2003, PASJ, 55, 75
Stanghellini, L., Magrini, L., Villaver, E., & Galli, D. 2010, A&A, 521, A3
Strong, A. W., & Mattox, J. R. 1996, A&A, 308, L21
Strong, A. W., Moskalenko, I. V., Reimer, O., Digel, S., & Diehl, R. 2004, A&A, 422, L47
Teuben, P. 1995, Astronomical Data Analysis Software and Systems IV, 77, 398
Thilker, D. A., Boissier, S., Bianchi, L., et al. 2007, ApJS, 173, 572
Thomas, H. C., Alexander, P., Clemens, M. S., et al. 2004, MNRAS, 351, 362
Tremonti, C. A., Heckman, T. M., Kauffmann, G., et al. 2004, ApJ, 613, 898
Vollmer, B., Soida, M., Chung, A., et al. 2008, A&A, 483, 89
Warmels, R. H. 1988, A&AS, 73, 453
Watanabe, Y., Sorai, K., Kuno, N., & Habe, A. 2011, MNRAS, 411, 1409
Wilson, C. D. 1995, ApJ, 448, L97
Zaritsky, D., Kennicutt, R. C., Jr., & Huchra, J. P. 1994, ApJ, 420, 87